

Large Histological Serial Sections for Computational Tissue Volume Reconstruction

U.-D. Braumann¹, N. Scherf¹, J. Einenkel², L.-C. Horn³, N. Wentzensen⁴,
M. Loeffler⁵, J.-P. Kuska⁶

¹Translational Centre for Regenerative Medicine, Leipzig, Germany

²Department of Obstetrics and Gynecology, University of Leipzig, Leipzig, Germany

³Institute of Pathology, University of Leipzig, Leipzig, Germany

⁴Division for Applied Tumour Biology, Institute of Pathology, University of Heidelberg, Heidelberg, Germany

⁵Institute for Medical Informatics, Statistics and Epidemiology, University of Leipzig, Leipzig, Germany

⁶Interdisciplinary Centre for Bioinformatics, University of Leipzig, Leipzig, Germany

Summary

Objectives: A proof of principle study was conducted for microscopic tissue volume reconstructions using a new image processing chain operating on alternately stained large histological serial sections.

Methods: Digital histological images were obtained from conventional brightfield transmitted light microscopy. A powerful nonparametric nonlinear optical flow-based registration approach was used. In order to apply a simple but computationally feasible sum-of-squared-differences similarity measure even in case of differing histological stainings, a new consistent tissue segmentation procedure was placed upstream.

Results: Two reconstructions from uterine cervix carcinoma specimen were accomplished, one alternately stained with p16^{INK4a} (surrogate tumor marker) and H&E (routine reference), and another with three different alternate stainings, H&E, p16^{INK4a}, and CD3 (a T-lymphocyte marker). For both cases, due to our segmentation-based reference-free nonlinear registration procedure, resulting tissue reconstructions exhibit utmost smooth image-to-image transitions without impairing warpings.

Conclusions: Our combination of modern nonparametric nonlinear registration and consistent tissue segmentation has turned out to provide a superior tissue reconstruction quality.

Keywords

Computer-aided image processing, uterine cervical diseases

Methods Inf Med 2007; 46: 614–622

doi:10.1160/ME9065

Introduction

The three-dimensional (3D) characterization of invasion patterns of squamous cell carcinoma of the uterine cervix is a current clinical question and is a matter of investigations with respect to prognosis [1]. Available 3D microscopic techniques for in-vivo or ex-vivo analyses include miniaturized computed tomography (μ CT), miniaturized nuclear magnetic resonance imaging (μ MRI), or confocal laser scanning microscopy (CLSM), etc. However, for reasonable specimen sizes (100 mm³ or more), and for a required degree of detail (about 10 μ m) either the applicable penetration range, the usable contrast or the spatial resolution exhibit substantial limitations. The modality we alternatively have decided to use is conventional bright-field transmitted light microscopy as it is basically applied in clinical routine, but have virtually extended it to 3D using *large histological serial sections* with up to several hundreds of slices. This in turn gives demand for high-level digital image processing as, for example, Ourselin et al. have introduced in their (rigid) approach intending to reconstruct brains of rats and rhesus monkeys [2]. Related methodologies for similar applications using reference-free registration approaches for 3D reconstruction of tissues were published by Bardin et al. [3], Lehmann et al. [4], Schormann and Zilles [5]. In part, other approaches have been tried to utilize reference volume data sets, i.e. ana-

tomical [6], metabolic [7], or atlas data [8]. Own work was focused on other histopathologic specimens (uterine cervix) which have required a cascade of reference-free registration steps to do an appropriate 3D tissue reconstruction. With the provided 3D microscopic data, and thanks to the applied nonparametric nonlinear registration based on optical flow, a new quality both for the 3D reconstruction and consequently for the morphological assessment of the considered tumor's invasion fronts was achievable [9].

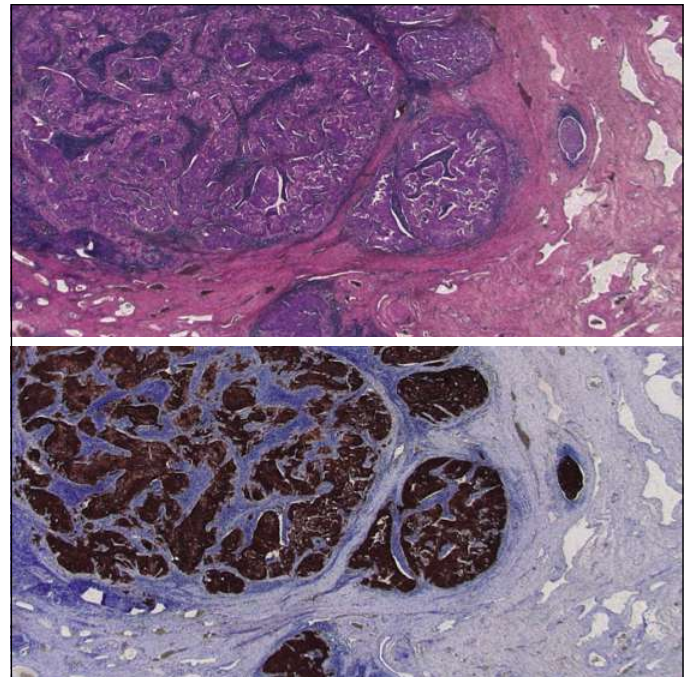
In this present work we demonstrate in a proof of principle the potential of our technology for *alternating histological stainings* for spatial co-localization using dedicated staining combinations, but without requiring laborious multiple-staining techniques for large serial sections. Generally, different staining of consecutive tissue sections can provide a valuable amount of additional information about the structure and position of different types of tissues. Especially, the combined use of different immunohistochemical stainings is expected to facilitate new insights e.g. into the interaction of cancer, inflammation and healthy cells in the human body. Multiple or even double-staining techniques using different immunohistochemical stains applied on one and the same section are rather difficult due to the interaction of the staining agents, and in many cases are not feasible. The solution we are proposing is the usage of consecutive sections (and series thereof), but with differ-

ent staining protocols accomplished on the separate slices.

What basically makes the registration of images of such sections difficult is the partial loss of spatial correspondences between the two sections. The reasons for the deformation between consecutive sections are not only due to some differences concerning the mechanical stress applied during the preparation, especially while sectioning. The partly aggressive chemical substances used for the staining usually cause some individual, non-uniform shrinkage of the different tissue types which may be comprised within a certain section. To reconstruct the spatial correspondences between the individual sections the usage of a basically non-linear registration procedure is required. The smaller the slicing and staining-originated distortions to be compensated, the more flexible adaptations a registration algorithm should allow for, and similarly, the higher precision demands concerning the underlying image data should be fulfilled, and vice versa. This also means that the registration method of choice is required to adequately treat the degree of deformation. In standard image processing toolboxes, like e.g. ITK, powerful nonparametric registration methods unfortunately are not included. As registration approach, we therefore consider a nonparametric partial differential equation approach, as was already successfully applied in our previous work [9], and similarly was suggested by others [10, 11].

The registration of differently stained images is not at all straightforward due to the fact that different stainings may exhibit totally different distributions both in color as well as in spatial location. However, since we deal with color images, the standard distance measure for multi-modal (i.e. unequal histological stainings in our case) image registration, the mutual information (MI) approach [12] unfortunately does not appear feasible, since the extent of required histograms for probability density estimates would be far beyond available RAM sizes on present computer systems. So, the direct usage of the color images for the registration process is not possible. Color space projections in order to provide secondary scalar (grayscale) image data would

Fig. 1
Images of two consecutive slices from a cervical carcinoma (case A) under H&E staining (top) and under p16^{INK4a} immunohistochemical staining (bottom). Image extents cover a region of approx. $8 \times 4 \text{ mm}^2$.



be too simple, since – for our cervical carcinoma cases – for one of the applied stainings the inflammatory margin appears almost indistinguishable from the tumor in e.g. the luminance image, so the wrong correspondences would manifest during the registration procedure. At this point, a certain processing step in order to emphasize some slight but important color differences is required. For a solution, it would be recommended not only to emphasize color differences, but to finally provide some scalar output in order to be able to apply some simple distance measure for the registration, and by this to circumvent MI even in this case (it anyway would be computationally expensive [13]). This is why we need to accomplish a segmentation step prior to the actual registration which, however, requires the utmost possible consistency referring to the various applied stainings. We consider this intermediate step essential in order to obtain the optimum accuracy for the respective registration transformation. Having done the segmentations at this point, there is no further need to segment after the subsequent registrations, as otherwise would be required in order to do quantitative analyses on the registered data.

Materials and Methods

Tissue Specimens, Histological Stainings, and Microscopic Image Digitization

For this proof of principle, two specimens were obtained from patients with cervical cancer which underwent radical hysterectomy. Case A was routinely classified as tumor stage pT2a, case B as pT1b1. Paraffin-embedded blocks were serially sliced (in radial direction; thickness: $10 \mu\text{m}$). Slicing and staining, however, unavoidably may induce severe artifacts, mainly different kinds of distortions. These should later be algorithmically compensated through nonlinear automatic image registration.

For case A, two distinct stainings were applied: Hematoxylin-eosin (H&E) and p16^{INK4a} (with hematoxylin as counterstain), which is an immunohistochemical (IHC) surrogate marker for an activated oncogene expression of high-risk type of human papillomaviruses (HPV), usually overexpressed in cervical carcinoma. While H&E is an unspecific routine method mainly highlighting regions with high relative cell nuclei densities as in tumor or

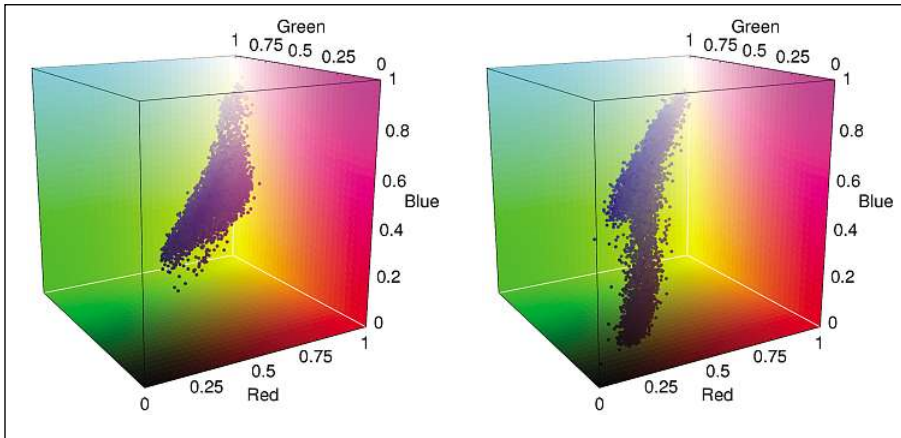


Fig. 2 Point clouds (corresponding to Fig. 1) representing all pixel color valences contained in the H&E (left) and the p16^{INK4a} image (right)

inflammation, p16^{INK4a} is expected to specifically mark just the tumor parts alone. For case B, we additionally applied another IHC marker, an anti-CD3 antibody which is considered a T-lymphocyte marker.

Digital images were taken on an upright bright-field transmitted light microscope (Zeiss Axioskop 2 plus). Images exhibit a standard size of 1300 × 1030 and have an effective spatial resolution of approx. 8 μm and cover an area of 0.865 cm². In order to ensure an optimum image quality, several settings were stipulated throughout image capturing, i.e. Köhler illumination, lamp current, damping filters, and diaphragm opening. Capturing software settings were considered to get a black reference image, to determine the correct white balance and to determine and apply the reference image for the shading correction.

The Correspondence Problem

A problem arises due to a partial loss of spatial correspondence between two respective images which possibly may exhibit totally different distributions both in the position (see Fig. 1) as well as in color space (see Fig. 2), unfortunately preventing the direct registration of the images. As a solution we introduce a *consistent image segmentation* step prior to the above mentioned nonlinear registration. For the intended registration (see below) we consider this step essential in order to obtain optimum accuracy.

Consistent Image Segmentation

The segmentation step plays the central role in the registration of slices with different staining, first in order to avoid causing misalignments and second to obtain scalar data in order to apply the sum of squared differences as distance measures and by this to avoid the mutual information thereof. We focus our interest on the statistical description of the distribution of pixel properties in a d -dimensional feature space. Every staining has an individual distribution in the used RGB color space. The identification of different tissue types does not only include

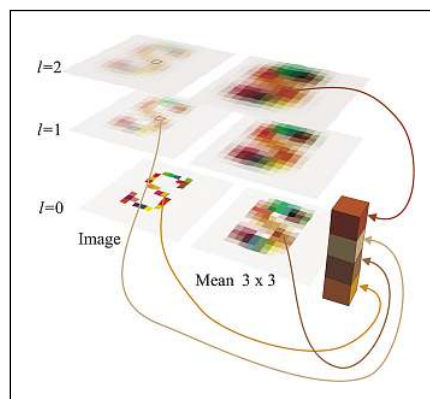


Fig. 3 Construction principle of the feature vector from the color, the mean, and the smoothing levels. In this example the segmentation vector is constructed from both the color of the original image and the Gaussian smoothed image, then the mean value of the unsmoothed and the two times smoothed image, giving a 3 × 4 dimensional segmentation vector.

pixel differences within the color space. The statistical properties of a pixel's neighborhood may also be important [14-16]. To include these properties into the segmentation, we construct a d -dimensional vector from selected statistical properties of the pixel (see Fig. 3). The neighborhood is included in the segmentation vector using properties such as the color mean value, and by the construction of successively smoothed images (denoted with the level index l in Fig. 3). Frequency properties of the respective pixel are included via sampling along an Archimedean spiral, starting at the respective pixel and analyzing the frequency distribution of a one-dimensional Fourier transform [17].

Based on the abovementioned feature vectors denoted as \vec{y}_i we basically apply a fuzzy c-means clustering method and estimate the parameters of an overall distribution

$$P(\vec{y}) = \sum_{k=1}^K \alpha_k p(\vec{y} | \vec{\mu}_k, \Sigma_k) \quad (1)$$

described as a linear combination of normal distributions $p(\vec{y} | \vec{\mu}, \Sigma)$ approximating the point clouds in the RGB color space (see Fig. 2). The estimation of the parameters $\vec{\mu}_k$, Σ_k and α_k is done using a variant of the expectation maximization (EM) algorithm [18, 19]. Using the estimated distribution $P(\vec{y})$ we assign a class number

$$c = \arg \max_k \frac{\alpha_k p(\vec{x} | \vec{\mu}_k, \Sigma_k)}{\sum_{i=1}^K \alpha_i p(\vec{x} | \vec{\mu}_i, \Sigma_i)} \quad (2)$$

to every pixel in the image and by this obtain the image segmentation. For the two slices in Figure 1 with *different* stainings we obtain two segmented images S and S' , whereas the class labels assigned by the algorithm are intended to be made *consistent* between the two segmentations. A typical reason therefore can be some inhomogeneous color saturation within one histological entity in one staining, while in the corresponding region of the adjacent, but differently stained section appears homogeneously. This means that the labels in one of the segmentations, say S' , normally will have to be exchanged to match the same regions as in the image S . The segmentation S' may have more classes K' than the segmentation S with K classes.

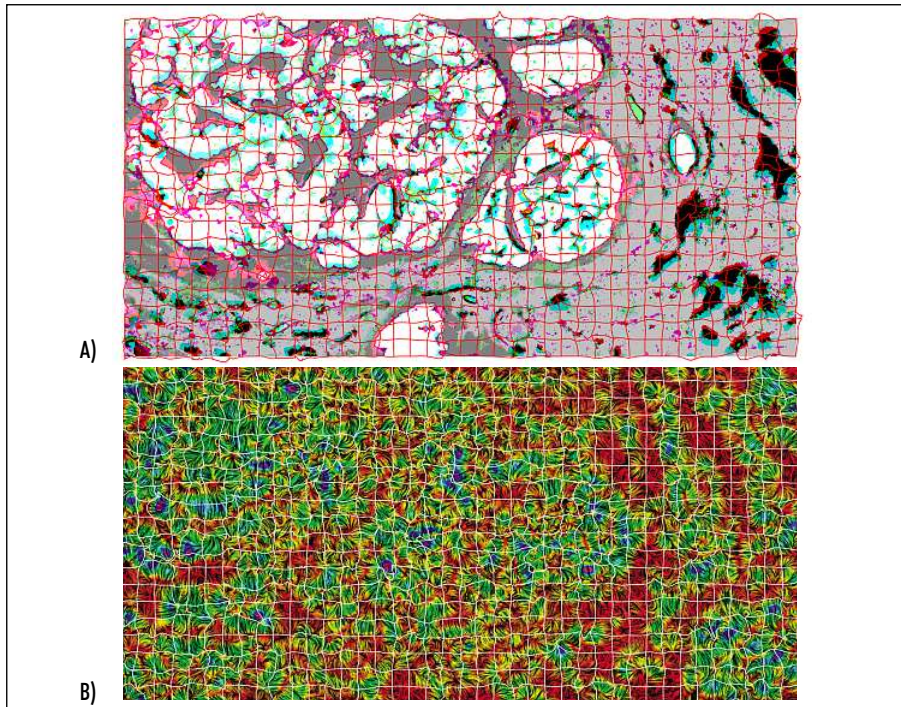


Fig. 4 A) Displacement field (red lines) obtained by the registration of the segmentations (see Fig. 6 bottom) of a p16^{INK4a} image (green RGB channel) onto an H&E-stained image (red RGB channel) with the transformed segmentation (blue RGB channel). Gray-valued regions appear where pairwise segmentations are consistent both before and after the registrations. Visible combination colors basically occur for the following reasons: Magenta and green margins denote regions where the p16^{INK4a} image was successfully aligned with the H&E image. A few cyan and reddish sites can be found where the p16^{INK4a} image failed to perfectly match with H&E. Yellow sites would mean that a mismatch would have been introduced by the transformation, but such regions practically do not occur. B) Corresponding image showing the displacement vector field as line integral convolution [21]

This could occur, for instance, when the second staining marks vessels that cannot be identified in the first staining. In such a case, the class labels must be merged to de-

scribe the same region in both segmentations. Merging of two or more classes is also required if – due to staining inhomogeneities – an accurate approximation of the

density distribution in color space would necessitate a superposition of several single multivariate normal distributions to describe the staining of one certain tissue type.

Image Registration

Once the segmentation was done for an image pair, we take the respective two scalar class label images to compute the displacement vector field $\vec{\mu}(\vec{x})$ for a nonlinear non-parametric registration based on optical flow. The latter will require the (numerical) solution of a coupled system of fourth-order partial differential equations: The computation of the displacement field $\vec{\mu}$ bases on the partial differential equation

$$\alpha \Delta^2 \vec{u}(\vec{x}) - \vec{f}(\vec{x}, \vec{u}(\vec{x})) = 0 \quad (3)$$

with

$$\vec{f}(\vec{x}, \vec{u}(\vec{x})) =$$

$$[S'(\vec{x}) - S(\vec{x} - \vec{u}(\vec{x}))] \nabla S(\vec{x} - \vec{u}(\vec{x})). \quad (4)$$

This equation was basically introduced in [10] and recently studied in [11] and [20], wherein Δ denotes the two-dimensional Laplace operator. To allow a smooth convergence for the solution, we introduce an artificial time t and solve the equation

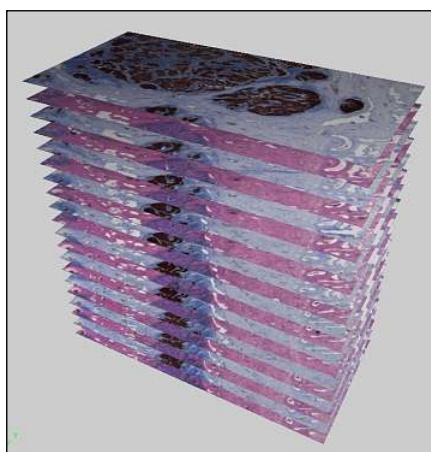


Fig. 5 First 20 images of case A, a serial section with an overall of 350 slices

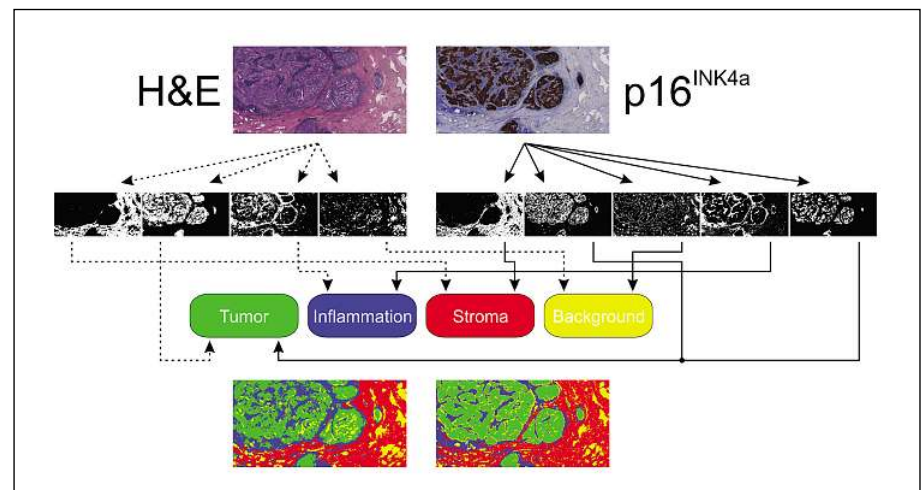


Fig. 6 Principle of the label exchange and label merging (black node) to obtain a consistent segmentation with four classes for an H&E and p16^{INK4a}-stained image pair from case A

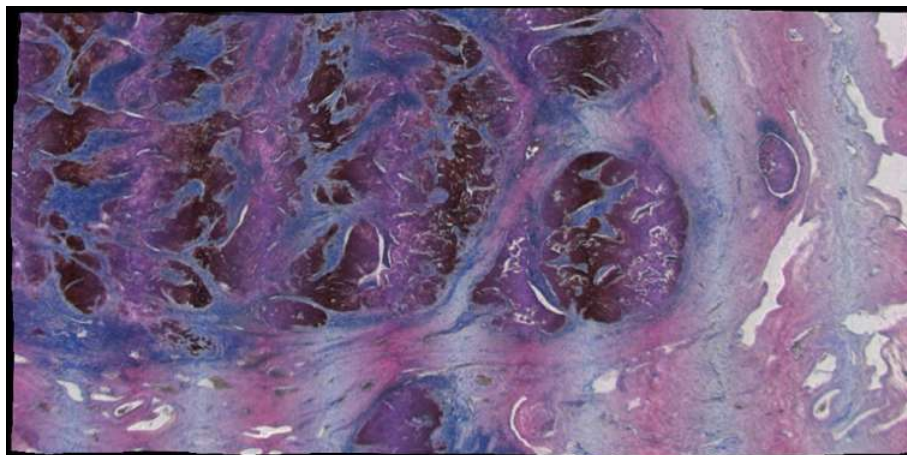


Fig. 7 Virtual plane through case A after the tissue reconstruction process: This image shows a plane with 1 degree tilt by this passing about 14 consecutive sections (the irregular outline is due to clipping of missing regions at neighboring slices after the applied registration procedures). While the tumor is more or less visible in all three stainings, it is best delimitable at the p16^{INK4a} slices as saturated brown structures. Due to the high accuracy of the obtained reconstruction, tumor structures as well as vessels and many other details smoothly continue in the adjacent slices. Image extents cover a region of approx. $8 \times 4 \text{ mm}^2$.

$$\frac{\partial \vec{u}}{\partial t}(\vec{x}, t) + \alpha \Delta^2 \vec{u}(\vec{x}, t) = \vec{f}(\vec{x}, \vec{u}(\vec{x}, t)). \quad (5)$$

The time discretization is done by an implicit midpoint rule and the dependence on

the position coordinate \vec{x} in the finite difference approximation of Δ^2 is resolved using a discrete cosine transform. A detailed description about the solution procedure and the used finite difference approximations can be found in [9]. Finally, when

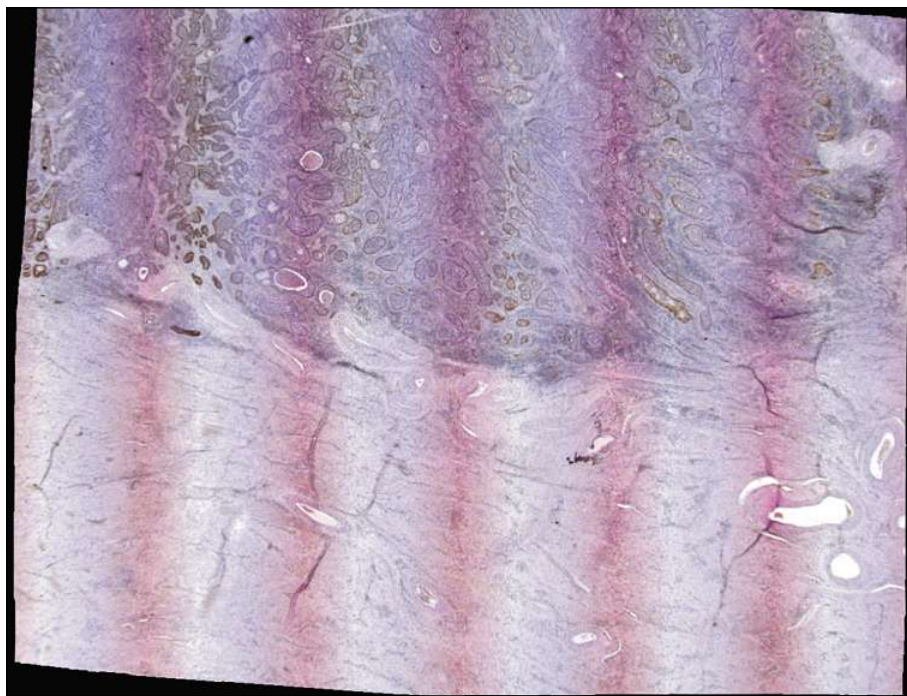


Fig. 8 Virtual plane through case B: Again, this image shows a plane with 1 degree tilt, by this passing about 17 consecutive sections. Right from each purple stripe (from H&E) follows p16^{INK4a} (cervical tumor marker) and then CD3 (T-lymphocyte marker). The expression of the latter is only moderate for this specimen. Like for case A (Fig. 7), the accuracy of the volume reconstruction gives smooth slice-to-slice transitions so that all tissue structures can be traced. Image extents cover a region of approx. $10 \times 7.7 \text{ mm}^2$.

the displacement field for the registration is found (see Fig. 4), the original color image is transformed according to this displacement field to obtain the registered version of the original data. For a whole set of images from a histological serial section, such displacement vector fields to successively register respective images onto their (previously registered) predecessors in the series are determined, so that – after hundreds of registration steps along one serial section – a reconstructed volume data set of the original image modality is obtained.

Results

For this proof of principle, the procedure outlined above was first applied to case A, consisting of an overall of 350 slices (see Fig. 5 for the first 20 slices), with the odd-numbered stained in H&E (routine stain) and the even-numbered in p16^{INK4a}. Main tissue types that appear in images of both parts are tumor, inflammation, and healthy stromal tissue, while of course H&E remains limited for good differentiation between tumor and inflammation. Further, due to visible vascular lumina or fissures, bright background regions are included. This suggests a total of four classes for the segmentation.

For the segmentation of H&E images, two smoothing levels $l = 1$ and $l = 2$ were used, and as features were chosen the color, the mean value in a 7×7 neighborhood of level $l = 0$ and the slope of the frequency distribution at $l = 1$. The p16^{INK4a} images were segmented using the color of both level $l = 0$ and $l = 1$. It has turned out that for p16^{INK4a} images an additional normal distribution is required to describe the color of the tumor region. While four classes were assumed above, for the H&E images we actually get four, but for the p16^{INK4a} five were obtained. Therefore, a reordering step was inserted at this point to merge the two classes both representing tumor (see Fig. 6 for a summary of the operations for one image pair). In practice, if the staining constancy is satisfactory along a series, it can be sufficient to both estimate the parameters of Equation 1 and do the interactive merging just based on the

properties of the first section image (“pilot image”) of one certain staining. By this, the segmentation process is considerably accelerated.

Following, the consistent segmentations obtained by these operations were used to compute the respective displacement fields required to accomplish the image registrations. For the depicted example pair in Figure 1, the p16^{INK4a} was transformed onto the H&E. In Figure 4 the result of this operation is depicted (see the figure caption for details).

After registering the whole serial section – the consistent segmentation of every slice was registered onto the consistent segmentation of its predecessor – a full 3D histological data set consisting of alternate stainings is ready for inspection. To outline the quality of the image registration obtained by the proposed method we show the result for this case A in Figure 7.

Further, the procedure outlined above was applied to case B, where a serial section with 84 consecutive slices from another cervical carcinoma was alternately stained with H&E as routine reference stain, with p16^{INK4a} labelling the cervical tumor cells, and additionally with CD3 in order to specifically detect T-lymphocytes. In analogy to Figure 7, Figure 8 illustrates the reconstruction result using a virtual plane. Now, the spatial relationship of the tumor invasion and the inflammatory response can be visually inspected interactively and further assessed quantitatively. Recently, this technology successfully could be extended to assess the shape of tumor invasion with respect to the T-cell infiltration [22].

In order to give a qualitative comparison of our procedure’s results with other parametric approaches, we refer to Figures 9 and 10, where reconstructed planes through the complete volume data sets are shown. Therein, for the purpose of comparison for our two cases A and B, additionally one example obtained from a rigid registration and one from nonlinear polynomial registration is given. Basically, what makes a quantitative assessment of the reconstruction performance difficult is the absence of some reference data set. One can visually compare the results of these two old methods with that from our new procedure de-

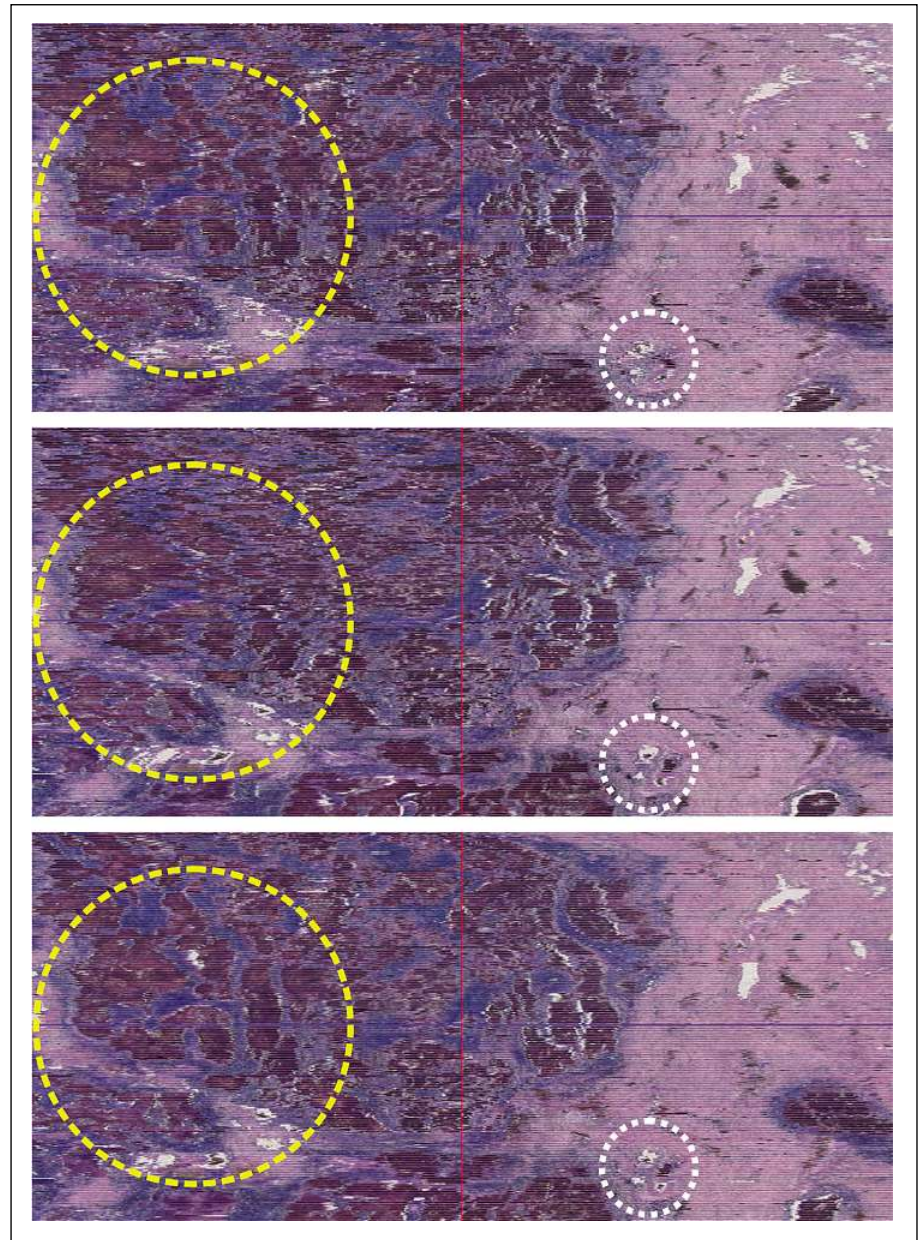


Fig. 9 Three corresponding virtual planes from case A with 90 degrees tilt passing all 350 sections (image extents approx. $7.8 \times 3.5 \text{ mm}^2$). While the topmost example was obtained by applying a rigid registration, the middle one results from a nonlinear polynomial registration. Comparing these two results of parametric registration with the lower result as was obtained with our approach described in this paper, the boundaries of the tumor (brown) clearly appear rather coarse, but not as smooth as with the new approach. E.g., for the area inside the large dashed yellow circle both the rigid and the polynomial approach, the tumor does not appear as smooth as in Figures 1 or 7 showing the same specimen. The small white dotted circle indicates some small vessels virtually cut in transversal direction partially with tumor inside. Here, the rigid approach (top) fails, while the results of the polynomial and the nonparametric approach appear comparable.

tailed in this paper. Looking at the structural details of Figures 9 and 10, and comparing them with Figures 1, 7 and 8, respectively, we illustrate the improvements in tissue volume reconstruction as can basically be obtained using nonlinear ap-

proaches. In particular, the examples illustrate the potential of the applied nonparametric nonlinear registration approach as underlying registration method for tissue reconstruction using large histological serial sections. Referring to some selected

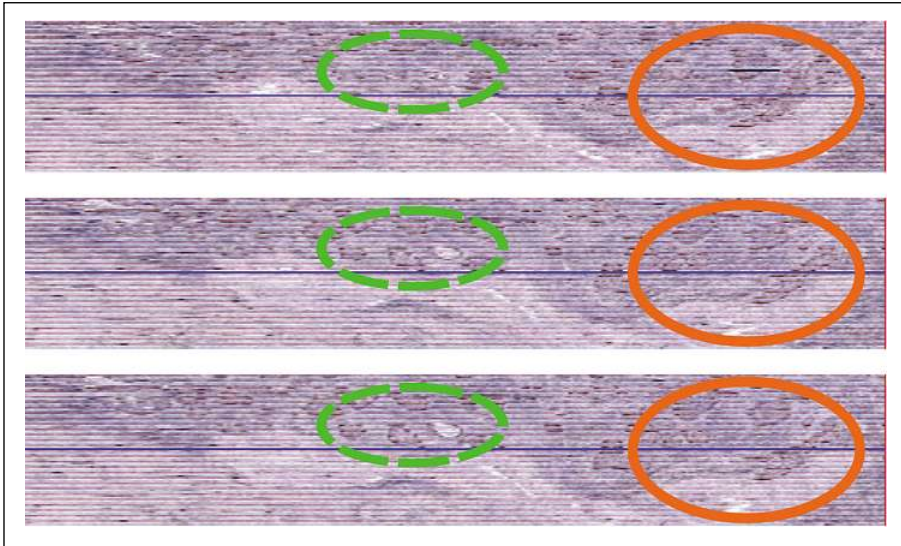


Fig. 10 Another three corresponding virtual planes from case B with 90 degrees tilt passing all 84 sections (image extents approx. $4.8 \times 0.84 \text{ mm}^2$). Due to three interleaving stainings, the structures are not as good recognizable as for case A in Figure 9. Again, the topmost example was obtained by applying a rigid registration and the middle one results from a nonlinear polynomial registration. The third result from the nonparametric nonlinear registration approach exhibits the smoothest margins for the tumor (brown), the inflammation (dark brown) as well as for the cavities (cp. the virtual plane in Fig. 8 from the same specimen). Looking at the dashed green ellipse, the enclosed tissue consists of tumor, normal stroma and some large vessel. These structures appear almost invisible in the rigid registration result, while the nonlinear polynomial and (even better) the nonparametric nonlinear approach do reconstruct these small structures quite precise. Similarly, the orange solid-line ellipse indicates an area wherein small tumor structures can be found. Again, the more sophisticated the approach, the better, clearer, and sharper the structures (with smooth boundaries due to smooth slice-to-slice transitions) appear.

areas the differences in the results are qualitatively discussed in the figure captions. The limitations of the nonparametric approach are seen in the image-global effect of the respective estimated parameter set,

whereas the degree of the polynomials cannot be arbitrarily raised without a considerable risk for unwanted warping. E.g. in the area to the right of the yellow ellipse in Figure 9 some small tumor structures appear

even worse in the reconstructed plane as with using the rigid approach alone! The nonparametric approach, however, with the results depicted at the bottom of Figures 9 and 10, can much better adapt to local misalignments in order to compensated most of them throughout the whole image.

Since for the two uterine cervix carcinoma cases, the tumor invasion front is of particular interest, Figures 11A and B, respectively, depict the segmented tumor surface (using an implementation of hardware-accelerated 3D volume rendering in this case) which can be interactively inspected for detailed analyses.

Discussion

We have demonstrated a procedure for tissue volume reconstruction utilizing a combination of consistent segmentation and nonparametric nonlinear registration for microscopic images of histological sections of different stainings. The method was successfully applied for a proof of principle study onto two cases (A and B), where the first is an alternating serial section H&E/p16^{INK4a} and the latter H&E/p16^{INK4a}/CD3. The results (esp. see Figs. 9 and 10) exemplify how the tissue volume reconstruction improves when compared to parametric approaches.

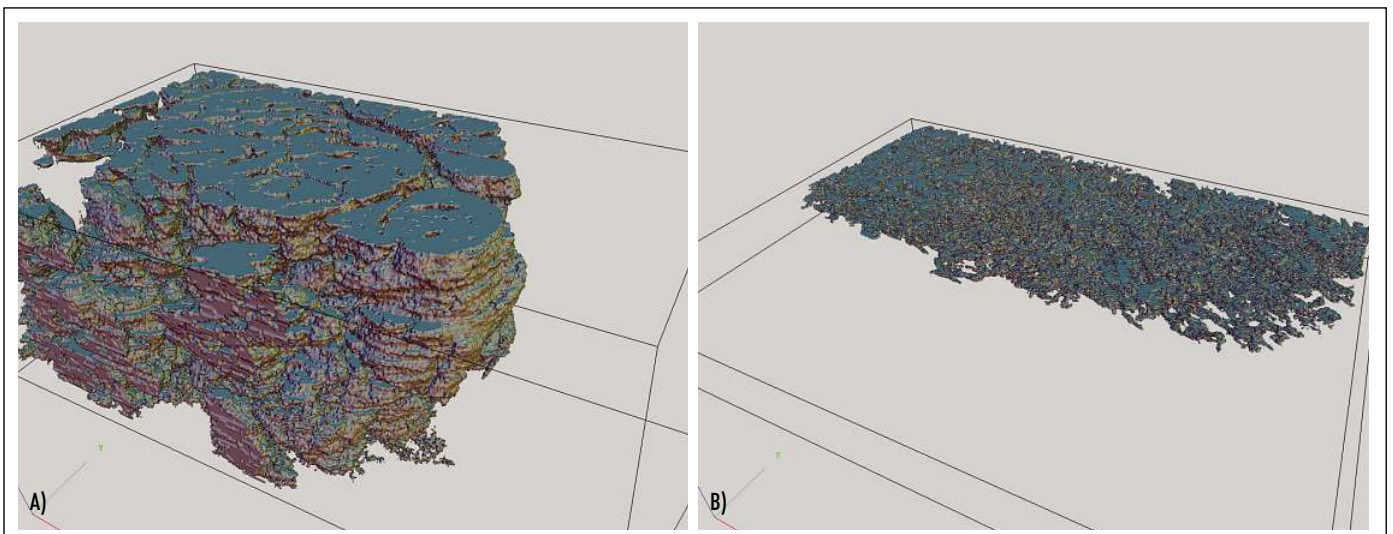


Fig. 11 3D visualizations of the segmented tumor invasion front for cases A and B, which clearly exhibit different patterns. For reasons of clearness, for this depiction only the major part of the respective tumor within the reconstructed volume is shown.

Gijtenbeek et al. [23] recently have published a method to 3D reconstruct cortical tumor microvasculature from serial sections. Their approach does not pay attention to the tumor tissue itself. They analyzed not only single-component-stained serial sections, but also double-alternating and double-stained sections. While the first was applied only to reconstruct the vessels using the endothelium marker CD34, the second and third method was accomplished additionally with smooth muscle actin. What was not applied is any counterstain, by this decisively simplifying the automatic segmentation step. However, it doesn't become obvious how the authors could manage the second method with double-alternating staining with their registration method using a normalized correlation metric to determine affine transforms. The latter may be sufficient for certain questions, however, better results will be obtained with non-linear approaches, since the underlying slicing-caused distortions are basically non-linear as well.

Palm et al. [24] have proposed a method to 3D reconstruct rat brain tumors using triple-alternating serial sections consisting of two different autoradiographs and some Cresyl-violet histological staining. The latter was separately registered as a reference stack, and in a second step the two autoradiographic data sets were then registered with their closest histological images within the sequence. They also have chosen normalized correlation, but just applied a rigid registration, by this taking even a higher loss of accuracy compared to Gijtenbeek et al. It can be assumed that the visible outline of the brain effectively was the most decisive registration criterion, so that a segmentation step prior to the registration was not required as was in our case.

Concerning our approach, the application of MI as a distance measure was not an option for the following reasons: The right side of Equation 4 represents the derivative of $\frac{1}{2} \int_{\Omega} S'(\vec{x}) - S(\vec{x} - \vec{u}(\vec{x}))^2 d\vec{x}$,

the sum of squared differences which serves as a distance measure here. However, MI is not differentiable in a similar way, but should be for the nonparametric differential

equation approach. Moreover, as mentioned above for color images as in our case, MI leads to extreme-sized histograms, which are not feasible for application, and generally would be computationally extremely expensive.

With the present work we would like to exemplify the potential for large serial section based 3D tissue volume reconstructions for histological analyses [25]. The reconstruction provides an accurate 3D tissue data set that allows performing quasi-seamless virtual oblique planes through the tissue "block". Using interactive software, the structures like the tumor can be viewed from all angles, substructures can be highlighted and interactions can be viewed. With our approach using large histological serial sections combined of different stainings we could demonstrate a powerful new technique for detailed 3D visualization and analysis of complex tissue intersections.

Concerning the registration procedure, comparing to the parametric registration approaches, the reconstruction using the non-parametric method using Equation 5 produces considerably higher computational expenses compared to the parametric approaches (processing times in the order of minutes instead of seconds), however – although a small drawback – in the framework of histological slide preparation and the digitization of hundreds of images this additional time requirement cannot be considered as a decisive bottleneck. For the consistent segmentation, which is the key for the usage of alternately stained serial sections, the merging step requires some user interaction. Fortunately, this can be done for the whole series in one step.

Even though the serial section based procedure may not be considered for clinical routine, it provides a practicable alternative for histology research. Going beyond our previous work [9] focusing on the 3D pattern of invasion for cervical tumors, we now could successfully demonstrate an important expandability of our technology for computational tissue volume reconstruction. In order to do a systematic evaluation of the proposed methodology, our work will continue with the application of this algorithm both on more cases and on larger VOIs and the inclusion of further stainings, e.g.

CD34 to analyze the microvascularization with respect to the tumor invasion front. Further aspects of tumor growth which basically can be detected with a similar approach are the tumor invasion-related expression of metalloproteinases.

References

1. Horn LC, Fischer U, Raptis G, Bilek K, Hentschel B, Richter CE, Braumann UD, Eienkel J. Pattern of invasion is of prognostic value in surgically treated cervical cancer patients. *Gynecologic Oncology* 2006; 103: 906-911.
2. Ourselin S, Roche A, Subsol G, Pennec X, Ayache N. Reconstructing a 3-D structure from serial histological sections. *Image and Vision Computing* 2001; 19: 25-31.
3. Bardinet É, Ourselin S, Malandain G, Tande D, Parain K, Ayache N, Yelnik J. Three dimensional functional cartography of the human basal ganglia by registration of optical and histological serial sections. *Proceedings of the IEEE International Symposium on Biomedical Imaging*; 2002 Jul 7-10; Washington DC, USA. IEEE; 2002; pp 329-332.
4. Lehmann TM, Goerke C, Kaupp A, Schmitt W, Reppes R. A rotation-extended cepstrum technique and its application to medical images. *Pattern Recognition and Image Analysis* 1996; 6: 592-604.
5. Schormann T, Zilles K. Limitations of the principal-axes theory. *IEEE Transactions on Medical Imaging* 1997; 16: 942-947.
6. Schormann T, Zilles K. Three-dimensional linear and nonlinear transformations: An integration of light microscopical and MRI data. *Human Brain Mapping* 1998; 6: 339-347.
7. Mega MS, Chen SS, Thompson PM, Woods RP, Karaca TJ, Tiwari A, Vinters HV, Small GW, Toga AW. Mapping histology to metabolism: Coregistration of stained whole-brain sections to pre-mortem PET in Alzheimer's disease. *Neuroimage* 1997; 5: 147-153.
8. Ali WSI, Cohen FS. Registering coronal histological 2-D sections of a rat brain with coronal sections of a 3-D brain atlas using geometric curve invariants and B-spline representation. *IEEE Transactions on Medical Imaging* 1998; 17: 957-966.
9. Braumann UD, Kuska JP, Eienkel J, Horn LC, Löffler M, Höckel M. Three-dimensional reconstruction and quantification of cervical carcinoma invasion fronts from histological serial sections. *IEEE Transactions on Medical Imaging* 2005; 24: 1286-1307.
10. Amit Y. A nonlinear variational problem for image matching. *SIAM Journal on Scientific Computing* 1994; 15: 207-224.
11. Fischer B, Modersitzki J. Curvature based image registration. *Journal of Mathematical Imaging and Vision* 2003; 18: 81-85.

12. Viola PA. Alignment by maximization of mutual information (dissertation). Cambridge (MA): Massachusetts Institute of Technology; 1995.
13. Haber E, Modersitzki J. Intensity gradient based registration and fusion of multi-modal images. *Methods Inf Med* 2007; 46: 292-299.
14. Manjunath BS, Ohm JR, Vasudevan VV, Yamada A. Color and texture descriptors. *IEEE Transactions on Circuits and Systems for Video Technology* 2001; 11: 703-715.
15. Lucchese L, Mitra SK. Color image segmentation: A state-of-the-art survey. *Proceedings of the Indian National Science Academy A (Physical Sciences)* 2001; 67: 207-221.
16. Manjunath BS, Ma WY. Texture features for browsing and retrieval of image data. *IEEE Transactions on Pattern Analysis and Machine Intelligence* 1996; 18: 837-842.
17. Scherf N. Segmentation of Tissue Structures in Brightfield Microscopy Images (diploma thesis). Leipzig: University Leipzig, Department of Computer Science; 2006.
18. Moon TK. The expectation-maximization algorithm. *IEEE Signal Processing Magazine* 1996; 13: 47-60.
19. Pernkopf F, Bouchaffra D. Genetic-based EM algorithm for learning Gaussian mixture models. *IEEE Transactions on Pattern Analysis and Machine Intelligence* 2005; 27: 1344-1348.
20. Braumann, UD, Kuska JP. Influence of the boundary conditions on the result of non-linear image registration. *Proceedings of the IEEE International Conference on Image Processing*; 2005 Sep 11-14; Genova, Italy. IEEE; 2005; pp I-1129-1132.
21. Cabral B, Leedom LC. Imaging vector fields using line integral convolution. *Proceedings of SIGGRAPH* 1993; 27: 263-272.
22. Wentzensen N, Braumann UD, Eienkel J, Horn LC, von Knebel Doeberitz M, Löffler M, Kuska JP. Combined serial section-based 3D reconstruction of cervical carcinoma invasion using H&E/p16^{INK4a}/CD3 alternate staining. *Cytometry* 2007; 71A: 327-333.
23. Gijtenbeek JMM, Wesseling P, Maass C, Burgers L, van der Laak JAWM. Three-dimensional reconstruction of tumor microvasculature: Simultaneous visualization of multiple components in paraffin-embedded tissue. *Angiogenesis* 2005; 8: 297-305.
24. Palm C, Dehnhard M, Vieten A, Pietrzyk U. 3D rat brain tumor reconstruction. *Biomedizinische Technik* 2005; 50 (Suppl. 1, Part 1): 597-598.
25. Eienkel J, Kuska JP, Horn LC, Wentzensen N, Höckel M, Braumann UD. Combined three-dimensional microscopic visualisation of tumour-invasion front of cervical carcinoma. *Lancet Oncology* 2006; 7: 698.

Correspondence to:

Ulf-Dietrich Braumann, Dr.-Ing.
University of Leipzig
Translational Centre for Regenerative Medicine
Philipp-Rosenthal-Straße 55
04103 Leipzig
Germany
E-mail: braumann@uni-leipzig.de